High-speed photo detection at two-micron-wavelength : technology enablement by GeSn/Ge multiple-quantum-well photodiode on 300 mm Si substrate

Xu, Shengqiang; Wang, Wei; Huang, Yi-Chiau; Dong, Yuan; Masudy-Panah, Saeid; Wang, Hong; Gong, Xiao; Yeo, Yee-Chia

2019

https://hdl.handle.net/10356/106411

https://doi.org/10.1364/OE.27.005798

High-speed photo detection at two-micron-wavelength: technology enablement by GeSn/Ge multiple-quantum-well photodiode on 300 mm Si substrate

SHENGQIANG XU,[1] **WEI WANG,**[1] **YI-CHIAU HUANG,**[2] **YUAN DONG,**[1] **SAEID MASUDY-PANAH,**[1] **HONG WANG,**[3] **XIAO GONG,**[1,4] **AND YEE-CHIA YEO**[1,5]

[1]*Department of Electrical and Computer Engineering, National University of Singapore 117576, Singapore*
[2]*Applied Materials Inc., Sunnyvale, California, United States*
[3]*School of Electrical and Electronic Engineering, Nanyang Technological University 639798, Singapore*
[4]*elegong@nus.edu.sg*
[5]*eleyeoyc@nus.edu.sg*

Abstract: We report high-speed photo detection at two-micron-wavelength achieved by a GeSn/Ge multiple-quantum-well (MQW) p-i-n photodiode, exhibiting a 3-dB bandwidth ($f_{3\text{-}dB}$) above 10 GHz for the first time. The epitaxy of device layer stacks was performed on a standard (001)-oriented 300 mm Si substrate by using reduced pressure chemical vapor deposition (RPCVD). The results showed promise for large-scale manufacturing. To our knowledge, this is also the first photodiodes-on-Si with direct radio-frequency (RF) measurement to quantitatively confirm high-speed functionality with tens of GHz $f_{3\text{-}dB}$ at 2 μm, which is considered as a promising candidate for the next data communication window. This work illustrates the potential for using GeSn to extend the utility of Si photonics in 2 μm band integrated optical transceivers for communication applications.

1. Introduction

Fiber-optic telecommunication system has been advancing continuously to satisfy the capacity demand from increasing volume of data transmission, enabled by many technologies breakthroughs like erbium-doped fiber amplifiers (EDFAs), wavelength division multiplexing (WDM), and high spectral efficiency coding. Conventional single mode fibers (SMFs) are approaching their theoretical capacity limit, which is related to the spectral efficiency of filling amplification bands of an EDFA [1]. Recent progress in low-loss hollow-core photonic band-gap fibers (HC-PBGFs) finds a lowest-loss window shift from 1.55 μm to around 2 μm, where a new and promising spectral window could be opened up for communication applications [2–4]. This may address the forecasted upcoming 'capacity crunch'. The theoretically predicted minimum loss is even lower than the conventional single mode fibers [5,6]. Thulium doped fiber amplifiers (TDFAs) with high gain and low noise at two-micron-wavelength window (1910-2010 nm) further enhance the feasibility of this new window to serve as a supplement to current telecommunication infrastructures.

Research effort has already been made to develop active components for 2 μm data communication. Si-based high-speed Mach-Zehnder interferometer (MZI) and ring modulators have been demonstrated recently on a standard 220 nm silicon-on-insulator (SOI) platform and the MZI modulator can operate at a data rate of 20 Gbit/s with an extinction ratio of 5.8 dB at 2 μm band [6]. Photo detectors are key components in optical receivers in fiber-optic communication networks and high speed functionality are highly desired. Photo detection currently covering this range is mainly based on III-V materials such as InP and

GaSb [7,8], which are difficult to integrate monolithically with Si photonics. High volume manufacturing is less likely due to the limited scalability of native III-V substrates. Although heterogeneous integration of III-V on Si through wafer-bonding or direct growth process has been explored to achieve on-chip photonic integrated circuits (PICs) [7–11], there has been no report on high speed III-V on Si photo detector operating at 2-μm range. Monolithic solution based on Group-IV materials could offer potential cost advantages and ease of integration with mainstream complementary metal-oxide-semiconductor (CMOS) technology. J. Ackert *et al.* reported a high speed Si-based photo detector at 2-μm range by introducing defects at mid-gap levels into Si-on-insulator waveguides through low-dose implantation of inert ions [12]. However, avalanche mode operation of this detector suffers from high reverse bias of 15 to 27 V and low response caused by weak interaction between sub-bandgap light and defects requires the device length to be several hundreds of micrometers. Ge photodiodes play a significant role in Si photonics based transceivers at conventional telecommunication bands. An elegant solution to address the photo detection issue at 2 μm is to develop the GeSn-based photodiodes to extend the Ge-based Si photonics to this new communication band. Recently, GeSn has attracted increasing attention due to its tunable direct bandgap and higher carrier mobilities, benefiting both electronics and photonics applications [13]. With a substitutional Sn (same group-IV element as Ge) concentration of ~6.5%, the absorption cut-off edge of Ge could be extended to ~2 μm [14]. Although GeSn-based photo detectors with enhanced sensitivity over traditional telecommunication bands have been demonstrated [15–17], so far, there is no report of high-speed functionality near two-micron-wavelength.

In this work, we demonstrate the first high speed GeSn/Ge multiple-quantum-well (MQW) photodiode with 3-dB bandwidth ($f_{\text{3-dB}}$) above 10 GHz at two-micron-wavelength. The complete active MQW layer stack was grown on a 300 mm (001)-oriented intrinsic Si substrate using a high quality 1 μm thick strain relaxed Ge buffer, showing great potential for large-scale manufacturing. Ultra-low leakage current density of 44 mA/cm^2 (at reverse bias of 1 V) was achieved, which is among the lowest reported values for all GeSn photodiodes and is even comparable to that of Ge photodiode. Extended photo sensitivity covering beyond 2 μm wavelength was demonstrated, significantly enhancing the detection capabilities of Ge-based Si photonics. GeSn/Ge MQW structure was employed to increase the critical thickness (h_c) of epitaxial GeSn on Ge virtual substrate. The substitutional Sn concentration in the GeSn quantum well is 8%. Quantum confinement effect in the GeSn quantum well will increase the effective bandgap of GeSn and thus blueshift the absorption cutoff. Therefore, six periods of relatively thicker GeSn quantum well with thickness of 25 nm were implemented in 35 nm thick Ge barriers in this work. Even with compressive strain and quantum confinement effect into consideration, our photodiode is predicted to have effective absorption cut-off (transition between first quantized energy levels of heavy hole and Γ-valley electron) of ~2.05 μm, covering the entire 2 μm window. This work illustrates the feasibility of GeSn-based photo detectors as a competent candidate for 2 μm band data communication.

2. Device design and material growth

The three-dimensional (3D) schematic of the surface-illuminated GeSn/Ge MQW photodiode is shown in Fig. 1. High quality 1 μm thick Ge buffer was first grown on the 300 mm (001)-oriented Si substrate as the virtual substrate for subsequent GeSn/Ge MQW device layer stack epitaxy. We noted that many Ge photo detectors are demonstrated on SOI, but the key for achieving high speed operation (especially for RC delay-limited devices) remains same: reducing parasitic capacitance as much as possible. We believe that both Si or SOI can be used as the starting substrate for technology demonstration. In order to achieve low substrate parasitic capacitance for realizing high speed operation in this work, the Si substrate with very low doping concentration (unintentionally-doped) in the range of 10^{14} cm^{-3} was used. Right after the Ge buffer growth, cyclic thermal anneal was conducted to reduce the threading dislocation density. The threading dislocation density that could penetrate to the Ge buffer

surface was controlled to be within the order of 10^7 cm^{-2} as measured from plane-view transmission electron microscopy (TEM). After that, the GeSn/Ge MQW structures were grown with digermane (Ge$_2$H$_6$) and tin tetrachloride (SnCl$_4$) as reactive gas precursors. The entire growth was performed using reduced pressure chemical vapor deposition (RPCVD) with heavily in-*situ* doped p$^+$- and n$^+$-contact layers (doping concentration higher than 10^{19} cm^{-3} for both p-type and n-type Ge contact layers).
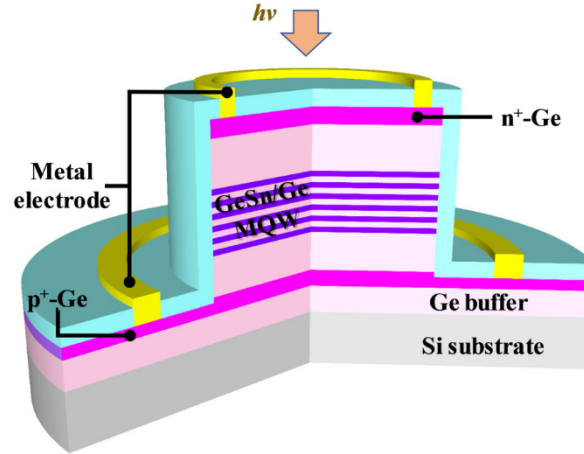

Fig. 1. Three-dimensional (3D) schematic of the GeSn/Ge MQW photodiode. GeSn/Ge MQW was inserted in the intrinsic Ge region as the active absorption layer as highlighted in purple color.

Although a thicker GeSn film with higher Sn composition is desired for enhancing the photo absorption, the material quality may degrade once its thickness exceeds the critical thickness, where strain relaxation occurs by forming misfits or threading dislocations. Misfit or threading dislocations act as recombination-generation centers and may increase the leakage current of the photodiodes. The critical thickness h_c of GeSn on Ge decreases with the increasing of Sn composition due to a larger lattice mismatch and could be predicted by People and Bean (P-B) model [18] using

$$h_c \simeq \left(\frac{1-v}{1+v}\right)\left(\frac{1}{16\pi\sqrt{2}}\right)\left[\frac{b^2}{a_{GeSn}}\right]\left[\left(\frac{1}{f^2}\right)\ln\left(\frac{h_c}{b}\right)\right], \tag{1}$$

where v is the Poisson ratio, which is calculated from the linear interpolation between that of Ge (0.273) and α-Sn (0.36), b is the Burger's vector magnitude (~0.4 nm), a_{GeSn} is the lattice constant of unstrained Ge$_{1-x}$Sn$_x$ calculated using $(1-x)a_{Ge} + xa_{Sn}$, x is the Sn concentration, f is the lattice mismatch given by

$$f = \frac{a_{GeSn} - a_{Ge}}{a_{Ge}}. \tag{2}$$

P-B model determines the critical thickness by comparing the areal strain energy density and self-energy density of an isolated dislocation of a given type (screw dislocation is usually taken as it has the minimum energy density). Figure 2 plots the critical thickness of GeSn on Ge virtual substrate. The effective critical thickness for MQW is estimated to have the same critical thickness for bulk GeSn with same effective Sn concentration. The effective Sn concentration is given by

$$x_{effective} = \frac{t_{well}}{t_{well} + t_{barrier}} x, \qquad (3)$$

where the well thickness t_{well} and barrier thickness $t_{barrier}$ are fixed at 25 and 35 nm, respectively, to mimic the real design. Figure 2 shows that the use of GeSn/Ge MQW structure instead of a single bulk GeSn layer could increase the effective critical thickness of epitaxial pseudomorphic GeSn [19]. In this work, the thickness of the epitaxial GeSn MQW is intentionally kept below the predicted value of h_c to ensure that it is fully strained to the strain-relaxed Ge buffer. This is the premise to enable good electrical and optical properties of the MQW. For further optimization, the ratio of the thickness of GeSn well to the thickness of the Ge barrier could be increased and a higher Sn concentration could be used to enhance the absorption and extend the absorption cut-off wavelength.
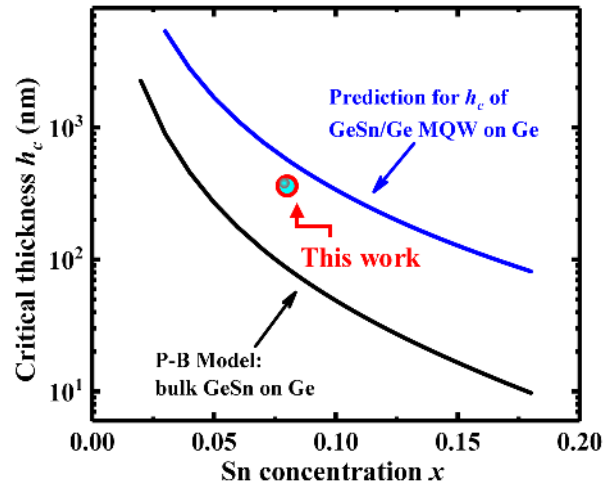

Fig. 2. Calculated critical thickness of bulk GeSn and GeSn/Ge MQW grown on Ge virtual substrate using People-Bean model. The thickness of the GeSn/Ge MQW in this work is also indicated as reference.

GeSn/SiGeSn MQW has been studied for its potential in lasing [20–22]. It could also be used for high-efficient light modulation based on quantum-confined Stark effect (QCSE) [23–25], although there is no experimental report so far. Growth of GeSn/SiGeSn MQW usually requires high quality strain relaxed GeSn buffer, which is difficult to achieve as compared to strain relaxed Ge buffer as high temperature anneal typically used to reduce defectivity cannot be applied on GeSn materials [26–28]. In addition, larger barrier height in GeSn/SiGeSn MQW may degrade the photodiode's high speed performance as the photon-generated carriers inside the GeSn quantum wells need to be transported out in order to reach contact regions. The escape time of photon-generated carries from a quantum well under electric field depends on thermal emission rate and tunneling rate. More dynamic studies performed on the GeSn MQW system are required to gain more insights. Shorter absorption cut-off wavelength is also expected for GeSn/SiGeSn as compared to bulk GeSn or GeSn/Ge MQW. Thus, GeSn/Ge MQW is employed here, which is favorable for photo detection as carrier confinement inside GeSn well is weaker when Ge is used as the barrier material.

The band diagram of the GeSn quantum well sandwiched by Ge barriers is investigated to evaluate the photo detection cut-off of the designed GeSn/Ge MQW photodiode. The quantum confinement effect is taken into consideration. Assuming no residual strain in the relaxed Ge buffer, its valence bands remain degenerate. The GeSn well is fully compressively strained to the Ge buffer. The compressive strain makes the heavy hole (HH) the topmost valence band in the GeSn well.

The bandgap of unstrained GeSn is first calculated using

$$E_{g,\eta}^{(Ge_{1-x}Sn_x)} = (1-x)E_{g,\eta}^{(Ge)} + xE_{g,\eta}^{(Sn)} - b_{\eta}^{GeSn}x(1-x), \tag{4}$$

where η refers to Γ or L conduction band valley, and b_{η}^{GeSn} is the bowing parameter with values of 2.42 and 0.99 eV for direct and indirect bandgap, respectively [29,30]. The energy shifts introduced by strain are modeled by deformation potential theory:

$$\Delta E_{HH} = a_v(2\varepsilon_{\parallel} + \varepsilon_{\perp}) + b_v(\varepsilon_{\parallel} - \varepsilon_{\perp}), \tag{5}$$

$$\Delta E_{LH} = a_v(2\varepsilon_{\parallel} + \varepsilon_{\perp}) - \frac{1}{2}b_v(\varepsilon_{\parallel} - \varepsilon_{\perp}) - \frac{1}{2}\Delta_0 + \frac{1}{2}\sqrt{\Delta_0^2 - 2\Delta_0 b_v(\varepsilon_{\parallel} - \varepsilon_{\perp}) + 9b_v^2(\varepsilon_{\parallel} - \varepsilon_{\perp})^2}, \tag{6}$$

$$\Delta E_c^{\eta} = a_c^{\eta}(2\varepsilon_{\parallel} + \varepsilon_{\perp}), \tag{7}$$

where $\varepsilon_{\parallel}$ is the in-plane strain, $\varepsilon_{\perp}$ is the normal strain, Δ_0 is the spin-orbit split-off energy, a_v and a_c are the hydrostatic deformation potential for valence and conduction band respectively, and b_v is the shear deformation potential. The $\varepsilon_{\parallel}$ and $\varepsilon_{\perp}$ in the GeSn well are defined as

$$\varepsilon_{\parallel} = \frac{a - a_{bulk}}{a_{bulk}}, \tag{8}$$

$$\varepsilon_{\perp} = -2\frac{C_{12}}{C_{11}}\varepsilon_{\parallel}, \tag{9}$$

where a is the in-plane lattice constant of the strained GeSn, and a_{bulk} is the lattice constant of GeSn without strain. C_{11} and C_{12} are the stiffness matrix elements. The band alignment was addressed by model-solid theory [31]. All the parameters used in this calculation are obtained by linear interpolation between that of Ge and α-Sn as summarized in Table 1, except the bandgap. Figure 3 shows the band alignment of the GeSn/Ge quantum well. The energy zero position is set at the average energy level of unstrained Ge valence bands. Theoretical calculation reveals that the compressively strained $Ge_{0.92}Sn_{0.08}$ well is still an indirect bandgap material and type I band alignment is obtained for both conduction and valence bands. The barrier offsets for electrons (ΔE^{Γ} and ΔE^L) and holes (ΔE^{HH} and ΔE^{LH}) are 0.089, 0.027, 0.116, and 0.022 eV, respectively.

The confined sub-band states in the quantum well are modeled by solving one dimensional time independent Schrödinger's equation

$$-\frac{\hbar^2}{2m^*(z)}\frac{\partial^2\phi_n}{\partial z^2} + V(z)\phi_n = E_n\phi_n, \tag{10}$$

where $\hbar$ is the reduced Planck constant, $m^*(z)$ is the carrier effective mass along the direction of interest (z-direction), $V(z)$ is the potential energy offset at the GeSn/Ge heterostructure interface, and E_n and ϕ_n are the eigenenergy and eigenfunction associated with the nth solution to this equation. For simplicity, the effective masses of electron at Γ-valley and heavy hole in [100] direction were taken from [13] with the value of 0.0316 and 0.223 m_0, without considering the effect of strain. The ground state energy for Γ-valley electron and heavy hole are calculated to be 0.0113 and 0.0022 eV with respect to the conduction and valence band edges of strained GeSn, respectively, as indicated with the dashed lines. Therefore, the designed photodiode has an effective photo absorption cut-off wavelength of ~2.05 μm, covering the working wavelength range of HC-PBGFs and TDFAs for 2 μm wavelength band data communication.
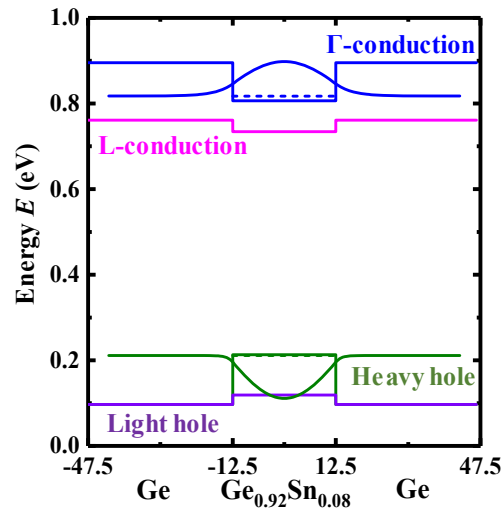
Fig. 3. Calculated band diagram for the GeSn well sandwiched by Ge barriers. Ground state energy was solved for Γ-valley electron and heavy hole as indicated with dashed lines. The wavefunctions for first quantized energy level of electrons and holes are also shown for reference.

Table 1. Parameters of Ge and α-Sn for Electronic Band Structure Calculation

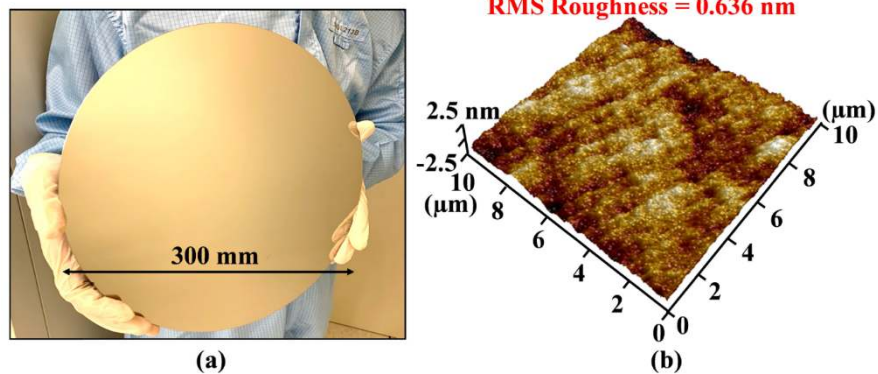|	Ge	α-Sn
a_{bulk} (Å)	5.6573[a]	6.4892[a]
$E_{v,ave}$ (eV)	0[a]	0.69[a]
Δ_0 (eV)	0.29[a]	0.8[a]
$E_{g,\Gamma}$ (eV)	0.7985[a]	−0.413[a]
$E_{g,L}$ (eV)	0.664[a]	0.092[a]
C_{11} (GPa)	128.53[a]	69[a]
C_{12} (GPa)	48.26[a]	29.3[a]
a_v (eV)	1.24[a]	−4.7[a]
b_v (eV)	−2.9[a]	−2.7[a]
a_c^{Γ} (eV)	−8.24[a]	−6[b]
a_c^{L} (eV)	−1.54[a]	−2.14[c]

[a] Ref [32], [b] Ref [33], [c] Ref [34].

Fig. 4. (a) Photograph image of the as-grown GeSn/Ge MQW on 300 mm Si substrate. High quality film with mirror-like surface was achieved across the whole wafer. (b) AFM image of the as-grown sample reveals a smooth surface with root-mean-square roughness of 0.636 nm for a scanning area of 10×10 μm^2.

The epitaxial growth of the device layers was performed as designed. Figure 4(a) shows the photograph image of the 300 mm as-grown GeSn/Ge MQW on Si substrate. Uniform film

with mirror-like surface was achieved across the entire 300 mm wafer. Figure 4(b) shows three-dimensional surface morphology of the as-grown sample obtained by atomic force microscopy (AFM). A smooth surface with root-mean-square (RMS) roughness of 0.636 nm was obtained for a scanning area of 10×10 μm^2. Transmission electron microscopy (TEM) was further performed to investigate the material quality. Figure 5(a) shows the cross-sectional TEM (XTEM) across the complete epitaxial layer stack. High-resolution TEM (HRTEM) image at the MQW region shown in Fig. 5(b) confirms the uniform periodicity of the GeSn wells and sharp transition between GeSn well and Ge barrier. No obvious threading dislocations were observed. Figure 5(c) shows a HRTEM image of the Ge/Si interface, where defects can be found to be effectively confined near the Ge/Si interface. A typical symmetric high-resolution X-ray diffraction (XRD) curve of the as-grown sample at (004) orientation is shown in Fig. 6(a). A series of satellite peaks from the periodic GeSn/Ge MQW can be clearly identified from the curve at lower 2 theta angles. The well-defined satellite peaks indicate the high crystalline quality of the GeSn/Ge MQW stack with good uniformity in epilayer thicknesses. Figure 6(b) shows the asymmetric (115) reciprocal space mapping (RSM) of the as-grown sample. The diffraction peak positions of the GeSn/Ge MQW and the relaxed Ge buffer are located at the same reciprocal lattice vector Q_x, revealing a coherent heterostructure and a fully compressively strained GeSn/Ge MQW on Ge virtual substrate.
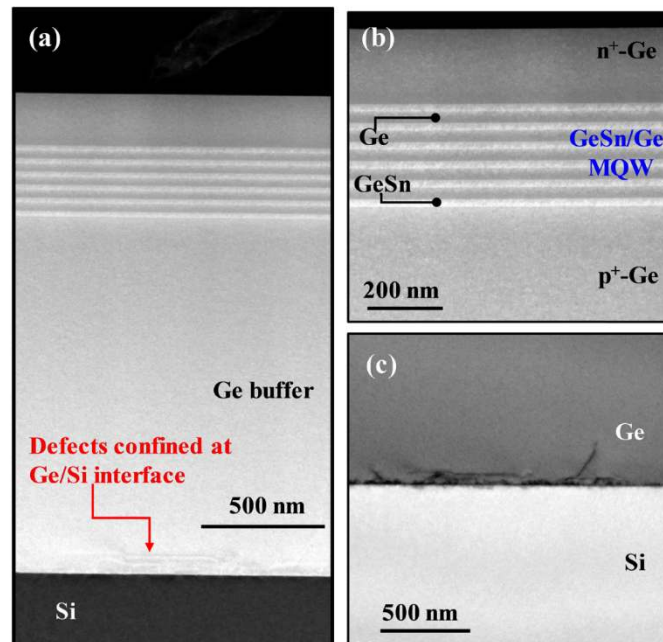

Fig. 5. (a) Cross-sectional TEM image of the entire epitaxial layer stack. (b) High resolution TEM clearly shows the quantum wells with sharp interface between GeSn and Ge. (c) Zoom-in view of the XTEM at the Ge/Si interface, where the defects are effectively confined.
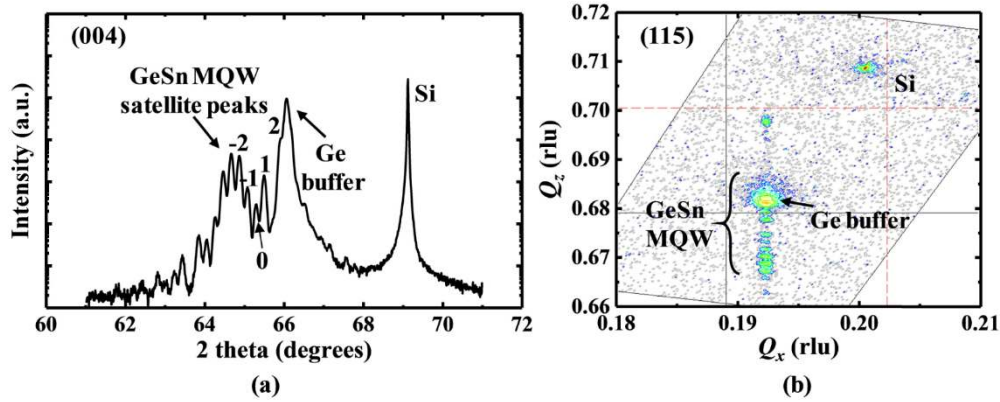
Fig. 6. (a) High resolution x-ray diffraction rocking curve of as-grown GeSn/Ge MQW sample at (004) orientation. MQW structure was revealed from the satellite peaks at lower 2 theta angles. (b) (115) reciprocal space mapping (RSM) of the as-grown sample. The GeSn/Ge MQW is fully strained to the strain-relaxed Ge buffer as indicated from the same in-plane lattice.
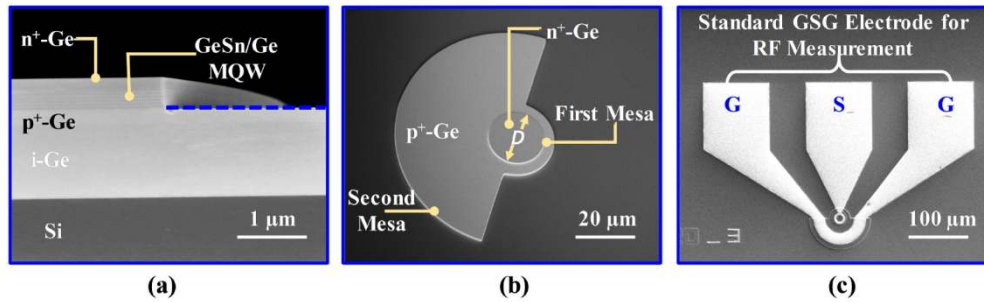

Fig. 7. (a) Cross-sectional SEM image of the GeSn/Ge MQW after first mesa patterning and dry etch. (b) Tilted-view SEM image of the GeSn/Ge MQW photodiode after forming the second mesa. (c) Top-view SEM image of one completed photodiode with standard GSG electrode.

3. Device fabrication and characterization

The GeSn/Ge MQW photodiode was realized using a double-mesa structure. The circular photodiode mesa was first patterned and formed by chlorine-based (Cl-based) inductive coupled plasma (ICP) etching. Mixed gases of Cl_2 and N_2 with gas flow rates of 10 and 3 sccm, respectively, were used for the ICP etching at a temperature of 150 °C and a pressure of 5 mTorr. Figure 7(a) shows the cross-sectional scanning electron microscopy (XSEM) image of the GeSn/Ge MQW mesa. The plasma etching was precisely time-controlled to stop on the p^+-Ge layer. Smooth mesa sidewall is observed. After that, the second mesa was formed using a fluorine-based (F-based) reactive ion etching (RIE) that exposed the Si substrate. This second mesa etch is critical for the realization of high speed photodiodes as it allows the electrode pads to be formed on the intrinsic Si substrate rather than the heavily-doped p^+-Ge so as to reduce the parasitic capacitance C_p [35,36]. Tilted-view SEM of the photodiode after the second mesa formation is shown in Fig. 7(b). After surface cleaning in hydrogen chloride (HCl) acid, a ~350 nm thick SiO_2 was then deposited as a passivation and isolation layer by plasma enhanced CVD (PECVD) at a temperature T of 250 °C. The contact region was then patterned and opened by dry etching followed by wet etching using diluted hydrogen fluoride (DHF) solution. Finally, aluminum (Al) electrodes were formed by sputtering and Cl-based ICP etch. The electrodes were designed in standard ground-signal-ground (GSG)

configuration with a pitch of 150 μm. Figure 7(c) shows the top-view SEM image of the finished photodiode with a diameter D of 20 μm.

Dark current is one of the key performance metrics for evaluating p-i-n photodiodes. The dark current determines the shot noise of the photodiode to a great extent as given by

$$i_s = \sqrt{2q(I_{ph} + I_d)B},\qquad(11)$$

where i_s is the total shot root-mean-square current, q is the electron charge, I_{ph} is the photocurrent, I_d is the dark current, and B is the bandwidth. Shot noise usually dominates the minimum detectable signal of a photodetector over thermal noise and $1/f$ noise [37]. The dark current-bias voltage (I_{dark}-V_{bias}) characteristics of the GeSn/Ge MQW photodiodes are shown in Fig. 8 with mesa diameters (D) ranging from 20 to 100 μm. The measurement was carried out at room temperature. Excellent rectifying behavior with high on/off ratio of ~1×10^4-1×10^5 was achieved for all photodiodes. The deviation in forward ($V_{bias} = 1$ V) current may be attributed to the variations in series resistance of each diode. A low dark current of 0.17 μA (~1 order lower than the typical 1 μA limit acceptable for high speed receiver design) was achieved for the photodiode with D of 20 μm at $V_{bias} = -1$ V.

Material defects and surface leakage are two causes for dark current. Their separate contribution is investigated here. The total dark current density J_{dark} can be formulated using

$$J_{dark} = J_{bulk} + \frac{4J_{surf}}{D},\qquad(12)$$

where J_{bulk} and J_{surf} are the bulk and surface leakage current density, respectively. Figure 9(a) shows the J_{dark} as a function of $1/D$ for the GeSn/Ge MQW photodiodes at reverse bias of 1 V. Both J_{dark} and J_{surf} are extracted from the linear fitting with a value of 42 mA/cm^2 and 5.7 μA/cm, respectively. Percentage of each leakage is then calculated and shown in Fig. 9(b). The slight increase of the surface leakage percentage for smaller dimension photodiodes is due to the increasing perimeter-to-area ratio. The low surface leakage density indicated good surface passivation in this work achieved by using HCl acid treatment and low-temperature PECVD SiO$_2$. It should be emphasized here that although the bulk leakage dominates the total leakage for all photodiodes, the total leakage density achieved in this work is among the lowest reported values for all GeSn on Si substrate p-i-n photodiodes as benchmarked in Fig. 10 [15,17,19,38–50]. It should also be noted that larger dark current density is generally expected for higher Sn concentration due to the reduced bandgap, which results in higher intrinsic carrier concentration and a higher tunnelling current.
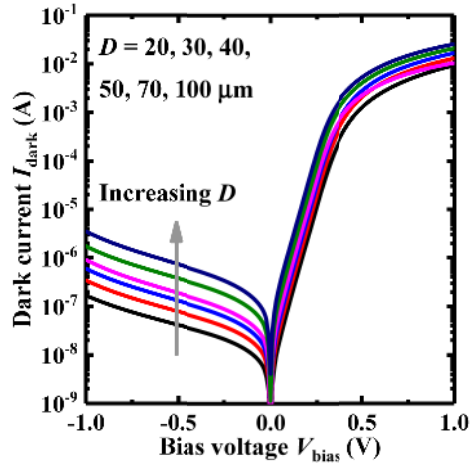
Fig. 8. Dark current-bias voltage (I_{dark}-V_{bias}) curves for the fabricated photodiodes with various mesa diameters (D).
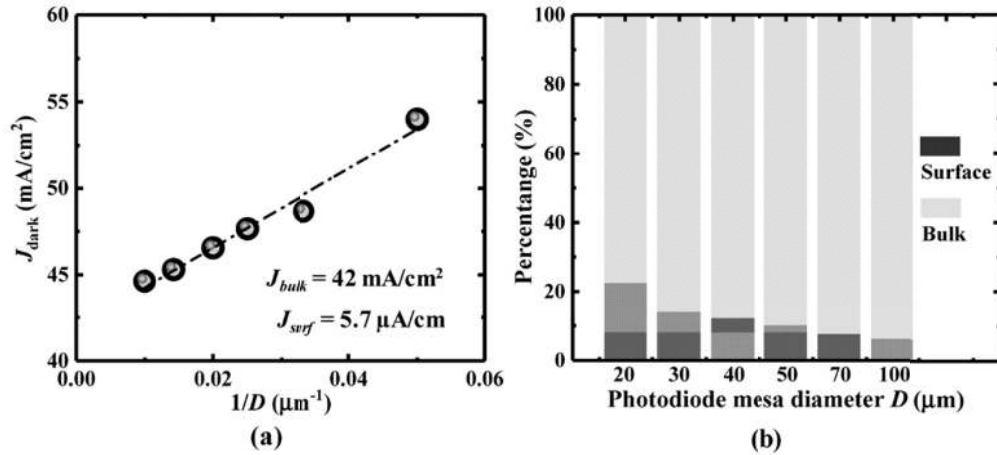

Fig. 9. (a) Dark current density J_{dark} versus $1/D$ of the photodiodes at a reverse bias of 1 V. Bulk leakage density J_{bulk} and surface leakage density J_{surf} can be extracted from a linear fit to the data. (b) Surface and bulk leakage percentage of the GeSn/Ge MQW photodiodes.
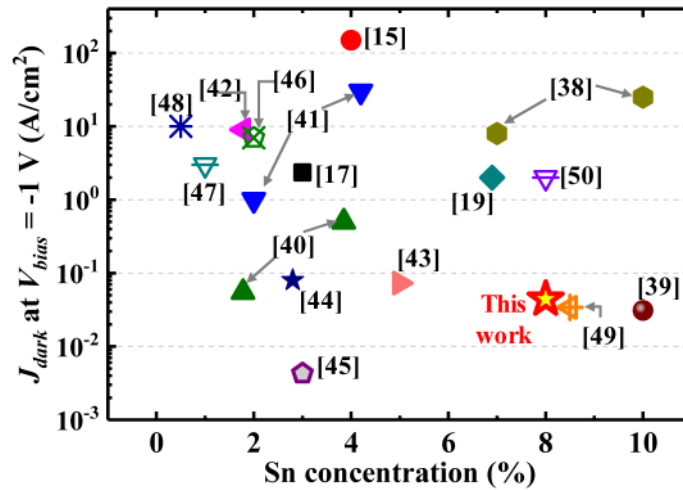
Fig. 10. Benchmarking of the dark current density J_{dark} for all GeSn on Si p-i-n photodiodes at reverse bias V_{re} of 1 V. A J_{dark} among the lowest reported values was achieved for a relative high Sn concentration of 8%.

The steady-state photo response characteristics of the GeSn/Ge MQW photodiode was measured in the wavelength range of 1550 - 2000 nm. Figure 11(a) presents the dark and illuminated current-bias voltage (I-V_{bias}) characteristics of the fabricated device with a mesa diameter of 40 μm at a wavelength of 1550 nm. The arrow indicates the direction of increasing incident light power P_{in}. The photocurrent increases linearly with P_{in} and no current saturation is observed. Flat photo response is also achieved even at zero bias, indicating good collection efficiency of photo-generated carriers. Photo response beyond the traditional communication band was investigated as shown in Fig. 11(b). Three distributed feedback laser diodes (DFB-LDs) with emission wavelengths of 1742, 1877, and 2000 nm were used for the optical measurement. P_{in} is fixed at 3.6 dBm. The photocurrent is reduced at higher wavelengths. Obvious photo sensitivity was observed to wavelengths up to 2 μm.
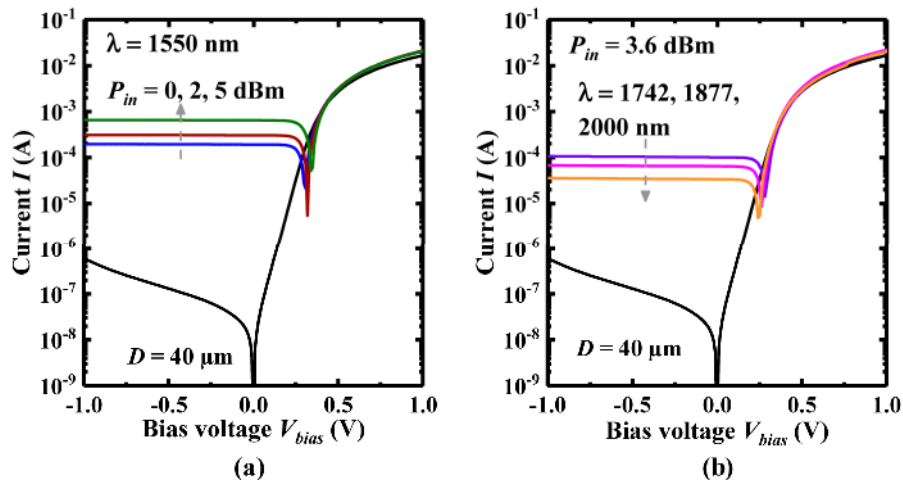

Fig. 11. (a) Current-bias voltage (I-V_{bias}) characteristics of the GeSn/Ge MQW photodiode at illumination wavelength of 1550 nm with incident power (P_{in}) of 0, 2, and 5 decibel milliwatts or dBm, respectively. (b) I-V_{bias} characteristics of the photodiode at illumination wavelength of 1742, 1877, and 2000 nm with a fixed incident power of 3.6 dBm, respectively. The photodiode under test has a mesa diameter (D) of 40 μm for facilitating the fiber alignment with the photodiode surface window.

Figure 12 shows the optical responsivity spectrum of the GeSn/Ge MQW photodiode at a reverse bias of 1 V from 1550 to 2000 nm. Conventional telecommunication bands (O to U-band) and the new 2 μm spectral band are indicated, showing the extended detection capabilities of our GeSn/Ge MQW photodiodes. Responsivity of 0.214, 0.047, 0.029, and 0.015 A/W were achieved for illumination wavelength of 1550, 1742, 1877, and 2000 nm, respectively. The decrease of responsivity at longer wavelengths is due to the decrease of absorption coefficients of GeSn and Ge. In addition, GeSn is considered as the only absorption material at 2 μm and the total absorption film thickness ($Ge_{0.92}Sn_{0.08}$ wells) is 150 nm in this work as designed within critical thickness to avoid strain relaxation. The photodiode responsivity could be further improved by introducing resonant cavities [51] or photon-trapping microstructures [52–54].
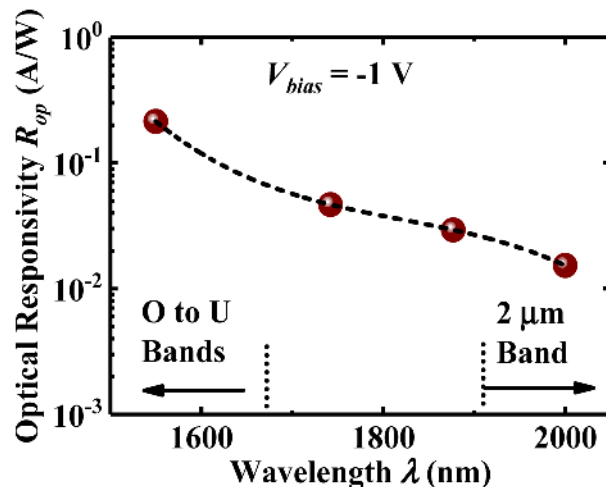

Fig. 12. Optical responsivity as a function of wavelength for the GeSn/Ge MQW photodiode ranging from 1550 to 2000 nm at a reverse bias (V_{re}) of 1 V. A detection cut-off beyond 2 μm can be clearly observed.

Radio frequency (RF) response of the GeSn/Ge MQW photodiode was investigated to explore its high speed operation potential for targeted communication applications. Figure 13 illustrates the optical testing setup of the RF measurement system at two-micron-wavelength. The light source used in this measurement was a fiber-coupled Fabry-Pérot laser diode (Thorlabs FPL2000S) at wavelength of 2000 nm. A polarization controller was implemented before the connection of the 10 GHz $LiNbO_3$ electro-optical (EO) Mach-Zehnder intensity modulator (Photline model MX2000-LN-10). The modulator was driven by the direct current (DC) and RF signal generated from a DC source meter and a vector networking analyzer (VNA, Agilent N5244A), respectively. The DC signal provided a stable bias voltage for intensity modulation at a certain operation point. The modulated light was guided to the surface window of the photodiode through a single-mode fiber (SMF). The coplanar GSG electrical input and output were connected to the second port of the VNA through a coaxial cable. A built-in bias tee was utilized to provide the DC supply to the photodiode. The measurements were calibrated to a commercial 2 μm InGaAs detector (ET5000) with a bandwidth larger than 12.5 GHz to de-couple the effect from modulator, cables, and other system components. Microscope image of one device under test (DUT) is shown in the inset of Fig. 13. The SMF is blurred as the image was taken with focus on the sample surface.
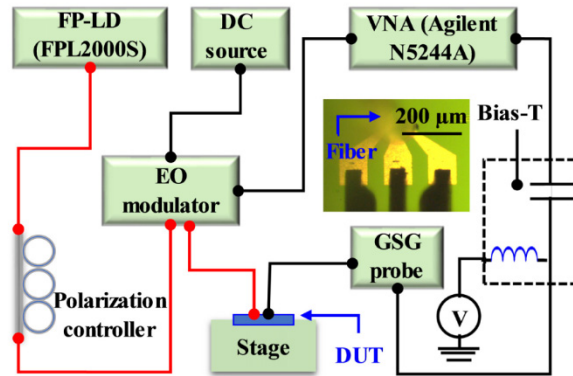
Fig. 13. Schematic of the experimental optical setup for the RF measurement of the GeSn/Ge MQW photodiode at two-micron-wavelength. The red and black lines indicate the optical and electrical connections, respectively. Inset shows the top-view microscopy image (with focus on sample surface) of the photodiode device under test (DUT), which has a mesa diameter of 20 μm.
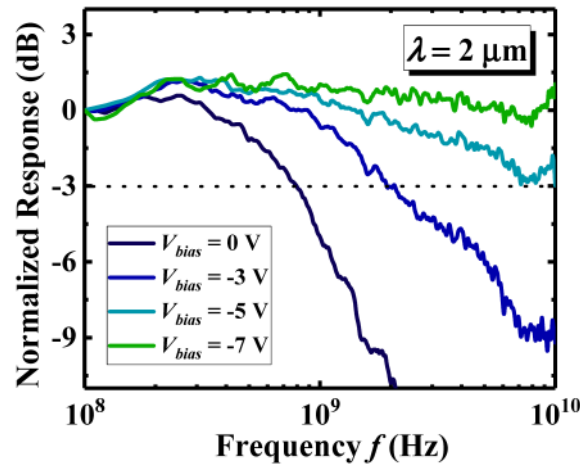

Fig. 14. Normalized small signal frequency response of the 20-m-diameter GeSn/Ge MQW photodiode at two-micron-wavelength. The bias voltage (V_{bias}) ranges from 0 to −7 V. At reverse bias larger than 5 V, the photodiode exhibits a 3-dB bandwidth beyond 10 GHz.

The small signal frequency response of the GeSn/Ge MQW photodiode with $D = 20$ μm is shown in Fig. 14, where the normalized response is plotted as a function of frequency. The 3-dB bandwidth f_{3-dB} increases with increasing the reverse bias. This could be due to the relatively high background doping of the epitaxial GeSn [41]. At low reverse bias, the intrinsic active region (GeSn/Ge MQW) is not fully depleted. This slows down the transit process of the photo generated carriers. Meanwhile, large junction capacitance (C_j) is expected, resulting in lower bandwidth at lower reverse bias. At a reverse bias of 7 V, photo detection beyond 10 GHz is achieved. The small signal frequency response here is an initial validation of the high speed operation. Due to the frequency limitation of the modulator used in the setup, it was not possible to measure the frequency response at higher speeds. The eye diagram is also not measured as limited by system capabilities. It should be noted that this is the first high speed (beyond 10 GHz bandwidth) photo detection directly characterized at $λ = 2$ μm. Future optimization in GeSn material growth to reduce the background doping will further enhance the device performance of GeSn-based photodiode.

4. Conclusion

For the first time, we demonstrated high speed photo detection beyond the conventional telecommunication bands and reaching the new promising two-micron-wavelength window realized by GeSn/Ge MQW photodiode monolithically integrated on Si substrate. Low leakage density of 44 mA/cm^2 is obtained at $V_{bias} = -1$ V, which is among the lowest reported values for all GeSn-on-Si photodiodes and is comparable to that of Ge-on-Si photodiodes. The photodiode shows capability to cover the new 2 μm spectral window. We expect significant improvement in responsivity by introducing resonant cavity or photon-trapping microstructures. 3-dB bandwidth higher than 10 GHz is experimentally demonstrated at two-micron-wavelength. This work paves way for using GeSn to extend the Ge-based Si photonics for high speed photo detection at 2 μm wavelength, which could be applied for the new telecommunication band.

References

1. D. Richardson, J. Fini, and L. Nelson, "Space-division multiplexing in optical fibres," Nat. Photonics **7**(5), 354–362 (2013).
2. P. J. Roberts, F. Couny, H. Sabert, B. J. Mangan, D. P. Williams, L. Farr, M. W. Mason, A. Tomlinson, T. A. Birks, J. C. Knight, and P. St. J. Russell, "Ultimate low loss of hollow-core photonic crystal fibres," Opt. Express **13**(1), 236 (2005).
3. E. Desurvire, C. Kazmierski, F. Lelarge, X. Marcadet, A. Scavennec, F. Kish, D. Welch, R. Nagarajan, C. Joyner, R. Schneider, Jr., S. Corzine, M. Kato, P. Evans, M. Ziari, A. Dentai, J. Pleumeekers, R. Muthiah, S. Bigo, M. Nakazawa, D. Richardson, F. Poletti, M. Petrovich, S. Alam, W. Loh, and D. Payne, "Science and technology challenges in XXIst century optical communications," C. R. Phys. **12**(4), 387–416 (2011).
4. H. Zhang, Z. Li, N. Kavanagh, J. Zhao, N. Ye, Y. Chen, N. Wheeler, J. Wooler, J. Hayes, S. Sandoghchi, F. Poletti, M. N. Petrovich, S. U. Alam, R. Phelan, J. O'Carroll, B. Kelly, D. J. Richardson, B. Corbett, and F. C. Garcia Gunning, "81 Gb/s WDM transmission at 2μm over 1.15 km of low-loss hollow core photonic bandgap fiber," in *ECOC*, 2014, pp. 5.20.
5. K. Nagayama, M. Kakui, M. Matsui, T. Saitoh, and Y. Chigusa, "Ultra-low-loss (0.1484 dB/km) pure silica core fibre and extension of transmission distance," Electron. Lett. **38**(20), 1168–1169 (2002).
6. W. Cao, D. Hagan, D. J. Thomson, M. Nedeljkovic, C. G. Littlejohns, A. Knights, S.-U. Alam, J. Wang, F. Gardes, W. Zhang, S. Liu, K. Li, M. S. Rouifed, G. Xin, W. Wang, H. Wang, G. T. Reed, and G. Z. Mashanovich, "High-speed silicon modulators for the 2 μm wavelength band," Optica **5**(9), 1055–1062 (2018).
7. N. Hattasan, A. Gassenq, L. Cerutti, J. Rodriguez, E. Tournié, and G. Roelkens, "GaSb-based integrated lasers and photodetectors on a Silicon-On-Insulator waveguide circuit for sensing applications in the shortwave infrared," in *IEEE PGC*, 2012.
8. R. Wang, M. Muneeb, S. Sprengel, G. Boehm, A. Malik, R. Baets, M.-C. Amann, and G. Roelkens, "III-V-on-silicon 2-μm-wavelength-range wavelength demultiplexers with heterogeneously integrated InP-based type-II photodetectors," Opt. Express **24**(8), 8480–8490 (2016).
9. S. Chen, W. Li, J. Wu, Q. Jiang, M. Tang, S. Shutts, S. N. Elliott, A. Sobiesierski, A. J. Seeds, I. Ross, P. M. Smowton, and H. Liu, "Electrically pumped continuous-wave III–V quantum dot lasers on silicon," Nat. Photonics **10**(5), 307–311 (2016).
10. Y. Wan, J. Norman, Q. Li, M. Kennedy, D. Liang, C. Zhang, D. Huang, Z. Zhang, A. Y. Liu, A. Torres, D. Jung, A. C. Gossard, E. L. Hu, K. M. Lau, and J. E. Bowers, "1.3 μm submilliamp threshold quantum dot micro-lasers on Si," Optica **4**(8), 940–944 (2017).
11. Y. Wan, Z. Zhang, R. Chao, J. Norman, D. Jung, C. Shang, Q. Li, M. J. Kennedy, D. Liang, C. Zhang, J.-W. Shi, A. C. Gossard, K. M. Lau, and J. E. Bowers, "Monolithically integrated InAs/InGaAs quantum dot photodetectors on silicon substrates," Opt. Express **25**(22), 27715–27723 (2017).
12. J. J. Ackert, D. J. Thomson, L. Shen, A. C. Peacock, P. E. Jessop, G. T. Reed, G. Z. Mashanovich, and A. P. Knights, "High-speed detection at two micrometres with monolithic silicon photodiodes," Nat. Photonics **9**(6), 393–396 (2015).

13. K. Lu Low, Y. Yang, G. Han, W. Fan, and Y.-C. Yeo, "Electronic band structure and effective mass parameters of Ge$_{1-x}$Sn$_x$ alloys," J. Appl. Phys. **112**(10), 103715 (2012).
14. W. Wang, Y. Dong, S.-Y. Lee, W.-K. Loke, D. Lei, S.-F. Yoon, G. Liang, X. Gong, and Y.-C. Yeo, "Floating-base germanium-tin heterojunction phototransistor for high-efficiency photodetection in short-wave infrared range," Opt. Express **25**(16), 18502–18507 (2017).
15. M. Oehme, M. Schmid, M. Kaschel, M. Gollhofer, D. Widmann, E. Kasper, and J. Schulze, "GeSn p-i-n detectors integrated on Si with up to 4% Sn," Appl. Phys. Lett. **101**(14), 141110 (2012).
16. J. Werner, M. Oehme, M. Schmid, M. Kaschel, A. Schirmer, E. Kasper, and J. Schulze, "Germanium-tin p-i-n photodetectors integrated on silicon grown by molecular beam epitaxy," Appl. Phys. Lett. **98**(6), 061108 (2011).
17. S. Su, B. Cheng, C. Xue, W. Wang, Q. Cao, H. Xue, W. Hu, G. Zhang, Y. Zuo, and Q. Wang, "GeSn p-i-n photodetector for all telecommunication bands detection," Opt. Express **19**(7), 6400–6405 (2011).
18. R. People and J. Bean, "Calculation of critical layer thickness versus lattice mismatch for Ge$_x$Si$_{1-x}$/Si strained-layer heterostructures," Appl. Phys. Lett. **47**(3), 322–324 (1985).
19. M. Oehme, D. Widmann, K. Kostecki, P. Zaumseil, B. Schwartz, M. Gollhofer, R. Koerner, S. Bechler, M. Kittler, E. Kasper, and J. Schulze, "GeSn/Ge multiquantum well photodetectors on Si substrates," Opt. Lett. **39**(16), 4711–4714 (2014).
20. D. Stange, N. Von den Driesch, D. Rainko, T. Zabel, B. Marzban, Z. Ikonic, P. Zaumseil, G. Capellini, S. Manti, J. Witzens, H. Sigg, D. Grützmacher, and D. Buca, "Quantum confinement effects in GeSn/SiGeSn heterostructure lasers," in *IEEE IEDM*, 2017, pp. 24.2. 1–24.2. 4.
21. D. Stange, N. von den Driesch, T. Zabel, F. Armand-Pilon, D. Rainko, B. Marzban, P. Zaumseil, J.-M. Hartmann, Z. Ikonic, G. Capellini, S. Mantl, H. Sigg, J. Witzens, D. Grützmacher, and D. Buca, "GeSn/SiGeSn Heterostructure and Multi Quantum Well Lasers," ACS Photonics **5**(11), 4628–4636 (2018).
22. N. von den Driesch, D. Stange, D. Rainko, I. Povstugar, P. Zaumseil, G. Capellini, T. Schröder, T. Denneulin, Z. Ikonic, J. M. Hartmann, H. Sigg, S. Mantl, D. Grützmacher, and D. Buca, "Advanced GeSn/SiGeSn Group IV Heterostructure Lasers," Adv. Sci. (Weinh.) **5**(6), 1700955 (2018).
23. Y.-H. Kuo, Y. K. Lee, Y. Ge, S. Ren, J. E. Roth, T. I. Kamins, D. A. Miller, and J. S. Harris, "Strong quantum-confined Stark effect in germanium quantum-well structures on silicon," Nature **437**(7063), 1334–1336 (2005).
24. P. Moontragoon, R. Soref, and Z. Ikonic, "The direct and indirect bandgaps of unstrained Si$_x$Ge$_{1-x-y}$Sn$_y$ and their photonic device applications," J. Appl. Phys. **112**(7), 073106 (2012).
25. N. Yahyaoui, N. Sfina, J.-L. Lazzari, A. Bournel, and M. Said, "Wave-function engineering and absorption spectra in Si$_{0.16}$Ge$_{0.84}$/Ge$_{0.94}$Sn$_{0.06}$/Si$_{0.16}$Ge$_{0.84}$ strained on relaxed Si$_{0.10}$Ge$_{0.90}$ type I quantum well," J. Appl. Phys. **115**(3), 033109 (2014).
26. R. Chen, S. Gupta, Y.-C. Huang, Y. Huo, C. W. Rudy, E. Sanchez, Y. Kim, T. I. Kamins, K. C. Saraswat, and J. S. Harris, "Demonstration of a Ge/GeSn/Ge quantum-well microdisk resonator on silicon: enabling high-quality Ge(Sn) materials for micro- and nanophotonics," Nano Lett. **14**(1), 37–43 (2014).
27. S. Takeuchi, Y. Shimura, O. Nakatsuka, S. Zaima, M. Ogawa, and A. Sakai, "Growth of highly strain-relaxed Ge$_{1-x}$Sn$_x$/virtual Ge by a Sn precipitation controlled compositionally step-graded method," Appl. Phys. Lett. **92**(23), 231916 (2008).
28. R. Chen, Y.-C. Huang, S. Gupta, A. C. Lin, E. Sanchez, Y. Kim, K. C. Saraswat, T. I. Kamins, and J. S. Harris, "Material characterization of high Sn-content, compressively-strained GeSn epitaxial films after rapid thermal processing," J. Cryst. Growth **365**, 29–34 (2013).
29. Y. Lin, Z. Jiang, X. Hu, X. Zhang, and J. Fan, "The electronic and optical properties of Eu/Si-codoped anatase TiO$_2$ photocatalyst," Appl. Phys. Lett. **100**(10), 102105 (2012).
30. I. A. Fischer, T. Wendav, L. Augel, S. Jitpakdeebodin, F. Oliveira, A. Benedetti, S. Stefanov, S. Chiussi, G. Capellini, K. Busch, and J. Schulze, "Growth and characterization of SiGeSn quantum well photodiodes," Opt. Express **23**(19), 25048–25057 (2015).
31. C. G. Van de Walle, "Band lineups and deformation potentials in the model-solid theory," Phys. Rev. B Condens. Matter **39**(3), 1871–1883 (1989).
32. S.-W. Chang and S. L. Chuang, "Theory of Optical Gain of Ge-Si$_x$Ge$_y$Sn$_{1-x-y}$ Quantum-Well Lasers," ," J. Quantum Electron **43**(3), 249–256 (2007).
33. Y.-H. Li, X. Gong, and S.-H. Wei, "Ab initio all-electron calculation of absolute volume deformation potentials of IV-IV, III-V, and II-VI semiconductors: The chemical trends," Phys. Rev. B Condens. Matter Mater. Phys. **73**(24), 245206 (2006).
34. T. Brudevoll, D. S. Citrin, M. Cardona, and N. E. Christensen, "Electronic structure of α -Sn and its dependence on hydrostatic strain," Phys. Rev. B Condens. Matter **48**(12), 8629–8635 (1993).
35. M. Oehme, K. Kostecki, K. Ye, S. Bechler, K. Ulbricht, M. Schmid, M. Kaschel, M. Gollhofer, R. Körner, W. Zhang, E. Kasper, and J. Schulze, "GeSn-on-Si normal incidence photodetectors with bandwidths more than 40 GHz," Opt. Express **22**(1), 839–846 (2014).
36. M. Gollhofer, M. Oehme, K. Kostecki, K. Ye, S. Bechler, K. Ulbricht, M. Schmid, M. Kaschel, R. Korner, W. Zhang, E. Kasper, and J. Schulze, "High speed vertical GeSn photodiodes on Si," in *IEEE GFP*, 2014, pp. 19–20.
37. L. Colace and G. Assanto, "Germanium on silicon for near-infrared light sensing," Photonics J. **1**(2), 69–79 (2009).

38. T. Pham, W. Du, H. Tran, J. Margetis, J. Tolle, G. Sun, R. A. Soref, H. A. Naseem, B. Li, and S.-Q. Yu, "Systematic study of Si-based GeSn photodiodes with 2.6 μm detector cutoff for short-wave infrared detection," Opt. Express **24**(5), 4519–4531 (2016).

39. Y. Dong, W. Wang, S. Xu, D. Lei, X. Gong, X. Guo, H. Wang, S.-Y. Lee, W.-K. Loke, S.-F. Yoon, and Y.-C. Yeo, "Two-micron-wavelength germanium-tin photodiodes with low dark current and gigahertz bandwidth," Opt. Express **25**(14), 15818–15827 (2017).

40. H. Tseng, H. Li, V. Mashanov, Y. Yang, H. Cheng, G. Chang, R. Soref, and G. Sun, "GeSn-based pin photodiodes with strained active layer on a Si wafer," Appl. Phys. Lett. **103**(23), 231907 (2013).

41. M. Oehme, K. Kostecki, K. Ye, S. Bechler, K. Ulbricht, M. Schmid, M. Kaschel, M. Gollhofer, R. Körner, W. Zhang, E. Kasper, and J. Schulze, "GeSn-on-Si normal incidence photodetectors with bandwidths more than 40 GHz," Opt. Express **22**(1), 839–846 (2014).

42. Y.-H. Peng, H. Cheng, V. I. Mashanov, and G.-E. Chang, "GeSn p-i-n waveguide photodetectors on silicon substrates," Appl. Phys. Lett. **105**(23), 231109 (2014).

43. Y. Dong, W. Wang, D. Lei, X. Gong, Q. Zhou, S. Y. Lee, W. K. Loke, S.-F. Yoon, E. S. Tok, G. Liang, and Y.-C. Yeo, "Suppression of dark current in germanium-tin on silicon p-i-n photodiode by a silicon surface passivation technique," Opt. Express **23**(14), 18611–18619 (2015).

44. Y.-H. Huang, G.-E. Chang, H. Li, and H. H. Cheng, "Sn-based waveguide p-i-n photodetector with strained GeSn/Ge multiple-quantum-well active layer," Opt. Lett. **42**(9), 1652–1655 (2017).

45. M. Morea, C. E. Brendel, K. Zang, J. Suh, C. S. Fenrich, Y.-C. Huang, H. Chung, Y. Huo, T. I. Kamins, K. C. Saraswat, and J. S. Harris, "Passivation of multiple-quantum-well Ge$_{0.97}$Sn$_{0.03}$/Ge p-i-n photodetectors," Appl. Phys. Lett. **110**(9), 091109 (2017).

46. J. Mathews, R. Roucka, J. Xie, S.-Q. Yu, J. Menéndez, and J. Kouvetakis, "Extended performance GeSn/Si (100) p-i-n photodetectors for full spectral range telecommunication applications," Appl. Phys. Lett. **95**(13), 133506 (2009).

47. J. Mathews, R. Roucka, C. Weng, R. Beeler, J. Tolle, J. Menéndéz, and J. Kouvetakis, "Near IR photodiodes with tunable absorption edge based on Ge$_{1-y}$Sn$_y$ alloys integrated on silicon," ECS Trans. **33**(6), 765–773 (2010).

48. J. Werner, M. Oehme, M. Schmid, M. Kaschel, A. Schirmer, E. Kasper, and J. Schulze, "Germanium-tin p-i-n photodetectors integrated on silicon grown by molecular beam epitaxy," Appl. Phys. Lett. **98**(6), 061108 (2011).

49. W. Wang, S. Vajandar, S. L. Lim, Y. Dong, V. R. D'Costa, T. Osipowicz, E. S. Tok, and Y.-C. Yeo, "In-situ gallium-doping for forming p$^+$ germanium-tin and application in germanium-tin p-i-n photodetector," J. Appl. Phys. **119**(15), 155704 (2016).

50. H. Cong, C. Xue, J. Zheng, F. Yang, K. Yu, Z. Liu, X. Zhang, B. Cheng, and Q. Wang, "Silicon based GeSn p-i-n photodetector for SWIR detection," Photonics J. **8**(5), 1–6 (2016).

51. B.-J. Huang, J.-H. Lin, H. H. Cheng, and G.-E. Chang, "GeSn resonant-cavity-enhanced photodetectors on silicon-on-insulator platforms," Opt. Lett. **43**(6), 1215–1218 (2018).

52. Y. Gao, H. Cansizoglu, S. Ghandiparsi, C. Bartolo-Perez, E. P. Devine, T. Yamada, A. F. Elrefaie, S.-y. Wang, and M. S. Islam, "High speed surface illuminated Si photodiode using microstructured holes for absorption enhancements at 900–1000 nm wavelength," ACS Photonics **4**(8), 2053–2060 (2017).

53. Y. Gao, H. Cansizoglu, K. G. Polat, S. Ghandiparsi, A. Kaya, H. H. Mamtaz, A. S. Mayet, Y. Wang, X. Zhang, T. Yamada, E. P. Devine, A. F. Elrefaie, S.-Y. Wang, and M. S. Islam, "Photon-trapping microstructures enable high-speed high-efficiency silicon photodiodes," Nat. Photonics **11**(5), 301–308 (2017).

54. H. Cansizoglu, C. Bartolo-Perez, Y. Gao, E. Ponizovskaya Devine, S. Ghandiparsi, K. G. Polat, H. H. Mamtaz, T. Yamada, A. F. Elrefaie, S.-Y. Wang, and M. S. Islam, "Surface-illuminated photon-trapping high-speed Ge-on-Si photodiodes with improved efficiency up to 1700 nm," Photon. Res. **6**(7), 734–742 (2018).